Room temperature ferrimagnetism, magnetodielectric and exchange bias effect in $CoFeRhO_4$

Prachi Mohanty,[1,*,†] Neha Sharma,[2,*] Deepak Singh,[1] Yohann Breard,[3] Denis Pelloquin,[3] Sourav Marik,[2,‡] and R. P. Singh[1,§]

[1]*Indian Institute of Science Education and Research Bhopal, Bhopal, 462066, India*

[2]*School of Physics and Materials Science, Thapar Institute of Engineering and Technology, Patiala 147004, India*

[3]*Laboratoire CRISMAT, UMR 6508 CNRS ENSICAEN, 6 bd du Marechal Juin, 14050 Caen Cedex 4, France*

(Received 27 April 2023; revised 10 July 2023; accepted 4 August 2023; published 22 August 2023)

Geometrically frustrated structures, combined with competing exchange interactions that have different magnitudes, are known ingredients for achieving exotic properties. Herein, we studied detailed structural, magnetic, thermal (specific heat), magnetodielectric, and magnetic exchange bias properties of a mixed $3d$-$4d$ spinel oxide with composition $CoFeRhO_4$. Detailed magnetization, heat capacity, and neutron powder diffraction studies highlight long-range ferrimagnetic ordering with an onset at 355 K. The magnetic structure is established using a ferrimagnetic model (collinear type) that has a propagation vector $k = 0$, 0, and 0. The magnetodielectric effect appears below the magnetic ordering temperature, and the exchange bias (EB) effect is observed in field-cooled conditions below 355 K. The magnetodielectric coupling in $CoFeRhO_4$ originates due to the frustration in the structure, collinear ferrimagnetic ordering, and uncompensated magnetic moments. The unidirectional anisotropy resulting from the uncompensated magnetic moments causes the room-temperature exchange bias effect. Remarkably, the appearance of technologically important properties (ferromagnetism, magnetodielectric effect, and EB) at room temperature in $CoFeRhO_4$ indicates its potential use in sensors or spintronics.

DOI: 10.1103/PhysRevMaterials.7.084408

I. INTRODUCTION

Spinel oxides are an intriguing class of materials not only for their potentiality for a wide range of applications, but also because of a variety of new and exciting physics (such as frustrated magnetism, multiferroic properties, orbital glass system, spintronics applications, and spin-orbital liquids) that continue to arise from the strong interactions among spin, orbital, and structural degrees of freedom [1–14]. They have a unique structure with a general formula of AB_2O_4, where A and B are metal ions (Fig. 1). This structure comprises an array of metal cations in octahedral and tetrahedral coordination, surrounded by oxygens, creating two sets of magnetic sublattices [15]. B cations generally form a pyrochlorelike lattice by residing in the octahedral sites and originate frustrated magnetic interactions [16–19]. On the other hand, metal A ions occupy the tetrahedral sites (eightfold) and construct a diamond lattice [21–25]. This bipartite lattice can be interpreted as two face-centered interpenetrated cubic sublattices. These sublattices are shifted diagonally by one-quarter. Variation of magnetic and nonmagnetic cations on the tetrahedral A sites and the octahedral B sites can originate complex magnetic interactions by affecting the magnitudes of superexchange interactions (J_{AA}, J_{BB}, and J_{AB}). Therefore, exotic properties (and states), such as a spiral spin liquid phase [26], unique, glassy magnetic behavior [22,27], and spin-orbital liquids [3,28] emerge in spinel materials. The pyrochlore lattice is a fertile playground for theoretical and experimental research to explore new physics. At the same time, the bipartite diamond lattice (in spinel systems) is a fruitful platform for realizing exotic quantum behavior. In particular, the bipartite nature of the diamond lattice can be useful in designing the recently proposed three-dimensional topological paramagnetism for the frustrated $S = 1$ diamond lattice [22,23].

In addition to geometrical frustration and competing exchange interactions having different magnitudes, spin-orbit coupling (SOC) is a known ingredient that favors more exotic spin order and dynamics. In this connection, $4d$ and $5d$ elements containing oxides have recently attracted great research interest. Being spatially more extended ($4d/5d$ orbitals), the on-site Coulomb repulsion energy (U) is smaller in $4d$ and $5d$ elements than their $3d$ analogs. However, in the spinel oxide family, only one $5d$-containing material has been reported so far. Spinel oxide containing iridium with composition $Cu[Ir_{1.5}Cu_{0.5}]O_4$ highlights a highly frustrated magnetic state [29]. Among the $4d$-rhodium-based diamond lattice spinel oxides, in the diamond-lattice Heisenberg antiferromagnet $CoRh_2O_4$, a combined experimental and theoretical work showed that the $S = 3/2$ spins are unfrustrated and exhibit static and dynamic properties [21]. Tetragonally distorted $CuRh_2O_4$ shows an incommensurate magnetic order for the $S = 1/2$ spins and the presence of sizable quantum effects [21]. A spin-orbit-entangled paramagnetic state is suggested in $NiRh_2O_4$ [22,27,30]. Studies on magnetically diluted $Cu_{1-x}Zn_xRh_2O_4$ highlight spin transition triggered by an enhancement of preceding spin fluctuations [31]. At the same time, it shows the suppression of orbital order

*These authors contributed equally to this work.

†Present address: Department of Physics, Odisha University of Technology and Research, Bhubaneswar, Odisha, 751003.

‡soumarik@thapar.edu

§rpsingh@iiserb.ac.in

on the octahedral sites in a percolative manner. In general, geometrically frustrated structures with $4d/5d$ elements (SOC) are ideal for realizing exotic phenomena. Therefore, exploring new frustrated structures (geometrical frustration and competing magnetic interactions) coupled with SOC is essential.

In this article, we present detailed structural (using x-ray powder diffraction, neutron powder diffraction, and electron microscopy), magnetic (magnetization), thermal (specific heat), and magnetodielectric studies on a mixed $3d$-$4d$ spinel oxide with composition $CoFeRhO_4$. In this material, nonmagnetic Rh^{3+} cations occupy octahedral B sites; however, they can be a source of SOC in the structure. An insulating and ferrimagnetic ground state is observed near room temperature (RT) ($T_C = 355$ K). Detailed magnetic and magnetodielectric measurements highlight the room-temperature exchange bias effect and the magnetodielectric effect in this material.

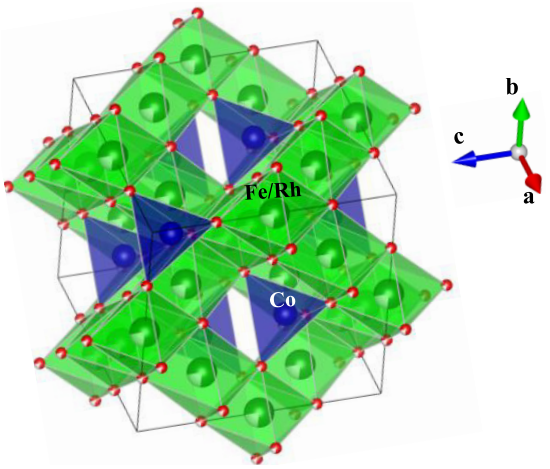

FIG. 1. Crystal structure for the $CoFeRhO_4$. Green spheres represent the Fe/Rh cations (octahedral B sites in the AB_2O_4 structure), Blue spheres represent the Co cations (tetrahedral A sites), and red spheres represent oxygen.

II. EXPERIMENTAL DETAILS

Synthesis. We have used the standard solid-state reaction route to synthesize polycrystalline $CoFeRhO_4$ materials. Stoichiometric amounts of Co_3O_4 (99.9%) Fe_2O_3 (99.999%), and Rh (99.9%) metal powders were used for synthesis. The stoichiometric amounts of the starting materials were mixed with a mortar pestle. The materials were heated several times, and the final sintering was performed at 1473 K for 36 h.

X-ray powder diffraction and neutron diffraction. X-ray diffraction (XRD) using the powder form of the material was collected at ambient temperature (RT) using a PANalytical diffractometer (Cu $K\alpha$, $\lambda = 1.540\,56$ Å). Neutron-diffraction (NPD) data for the powdered $CoFeRhO_4$ sample were collected at various temperatures (12, 100, and 250 K) at the JEEP II, Kjeller Reactor, Norway ($\lambda = 1.5538$ Å). We have performed the Rietveld refinements of the diffraction patterns (XRD and NPD) using the FULLPROF suite software.

Electron microscopy. We have performed electron microscopy measurements (high-angle annular dark-field scanning transmission electron microscopy (HAADF-STEM) and electron diffraction) to explore the crystal structure of $CoFeRhO_4$. HAADF-STEM and electron diffraction were carried out using a JEOL ARM-200F cold field-emission electron gun probe image aberration corrected 200-kV microscope. The instrument is also equipped with a solid-angle CENTURIO EDX detector.

Magnetism and specific heat. Direct current magnetization (temperature and magnetic-field-dependent) measurements were performed in a Quantum Design superconducting quantum interference device 3. Magnetic measurements were conducted in field-cooled (FC) and zero-field-cooled (ZFC) modes. Specific heat was measured (2–400 K) in a physical property measurement system (PPMS, Quantum Design) without a magnetic field.

Dielectric measurements. The temperature and magnetic-field-dependent dielectric measurements were performed using an LCR meter (Agilent 4284A) and a sample insert for a PPMS (Quantum Design).

III. RESULTS AND DISCUSSION

Preliminary Rietveld refinement uses the room-temperature XRD pattern of $CoFeRhO_4$. It shows that the sample crystallizes in a cubic structure with a space-group $Fd\bar{3}m$, which is isostructural with $CoFe_2O_4$ [32,33]. However, a small amount of Rh is detected [main peak at $2\theta \simeq 41^\circ$, Fig. S1 in the Supplemental Material (SI)] [20] in the RT XRD pattern for $CoFeRhO_4$. Furthermore, to explore the detailed nuclear and magnetic structure, we have collected the NPD patterns at 12, 100, and 250 K. Therefore, we will use the results of the NPD Rietveld refinements to describe the crystal structure of $CoFeRhO_4$. Similar to the XRD pattern, a small amount of Rh is also detected in the NPD patterns. Figure 2 illustrates the plot of the NPD Rietveld refinement for the pattern collected

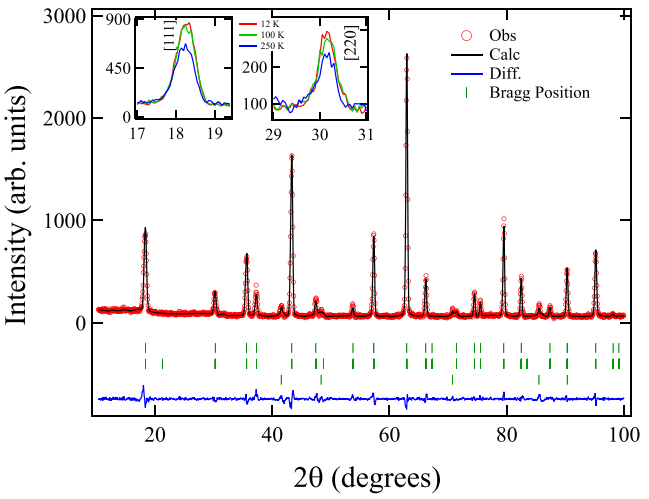

FIG. 2. Rietveld refinement plot of the NPD pattern collected at 12 K for $CoFeRhO_4$. The lower ticks highlight the magnetic peak positions ($k = 0, 0$, and 0). Insets in the figure show the enhancement of the [111] and [220] NPD peaks with a lowering of the temperature.

TABLE I. Structural parameters for $CoFeRhO_4$ at RT extracted from Rietveld refinement of powder XRD diffraction data.

Space group $Fd\bar{3}m$, $a = b = c = 8.4207$ (1) Å
$R_P = 6.98$, $R_{WP} = 9.01$, $\chi^2 = 1.03$, $R_{\text{Bragg}} = 2.79$
$R_{Mag} = 5.29$, M (T_d) $= 3.4(1)\mu_B$, M (Oct.) $= 4.1(1)\mu_B$

Atom	Wyck. Pos.	x	y	z	Occu.	B_{iso}
Co(T_d)	8a	0.125	0.125	0.125	0.88 (2)	0.1 (1)
Fe(T_d)	8a	0.125	0.125	0.125	0.12(2)	0.1(1)
Co(Oct.)	16d	0.5	0.5	0.5	0.065(5)	0.11(3)
Fe(Oct.)	16d	0.5	0.5	0.5	0.44(1)	0.11(3)
Rh(Oct.)	16d	0.5	0.5	0.5	0.49(1)	0.11(3)
O	32e	0.249(1)	0.249(1)	0.249(1)	1	0.10(3)

at 12 K. The plots of the NPD Rietveld refinements for the patterns collected at different temperatures are provided in the supporting information (Fig. S2 in the SI) [20]. The structural parameters obtained from the 12 K–NPD refinement for $CoFeRhO_4$ are summarized in Table I. The crystal structure of $CoFeRhO_4$ is highlighted in Fig. 1. Rh atoms and most of the Fe cations occupy the structure's octahedrally coordinated B site [16d (0.5, 0.5, 0.5)]. Co cations occupy the eightfold tetrahedral A sites [8a (0.125, 0.125, 0.125)]. Oxygen atoms occupy the 32e (x, x, and x) Wycoff positions. Refinement of oxygen occupancy indicates no deviation from the full occupancy. Rh shows a slight deviation from full occupancy [occupancy = 0.98 (2)]. Figure 3 shows the STEM-HAADF image along the [011] direction for $CoFeRhO_4$. The observed STEM images agree with the expected crystal structure of the spinel material. The lattice parameter obtained from STEM images (8.4 Å) matched the values found from the NPD (Table I) and RT-XRD refinements.

The structural (Rietveld) refinement of the 250 K NPD highlights the existence of magnetic peaks at that temperature. These magnetic-ordering-related peaks show an increase in intensity with decreasing temperature (inset in Fig. 2). The position of all magnetic peaks for $CoFeRhO_4$ coincides with the allowed nuclear reflections. Therefore, we describe the magnetic structure using the propagation vector $k = (0,0,0)$. The best fit to the NPD magnetic reflections for long-range magnetic order is achieved using a collinear ferrimagnetic

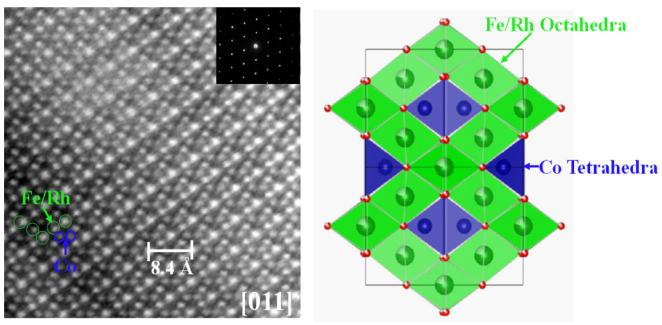

FIG. 3. HAADF image and crystal structure along the [011] zone axis for $CoFeRhO_4$, collected at room temperature. Fe, Rh, and Co cations are highlighted in the figure. The corresponding electron diffraction pattern is shown in the inset.

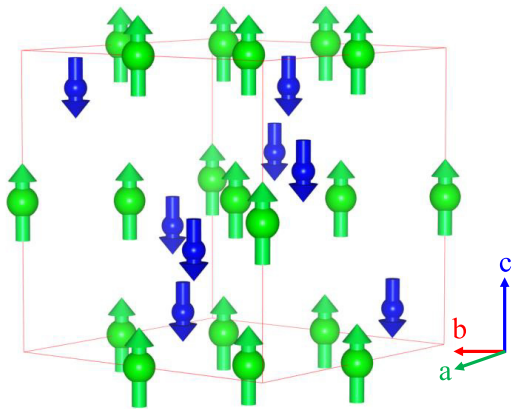

FIG. 4. The observed magnetic structure (k = 0, 0, 0) for $CoFeRhO_4$. A collinear ferrimagnetic ordering scheme is observed in the NPD refinements. The NPD refinement does not provide any indication on the direction of ordering (cubic magnetic unit cell). The magnetic moments can be ordered along any of the three-unit-cell vectors (a–c).

ordering model (Fig. 4). A similar magnetic-ordering scheme was proposed for the $CoFe_2O_4$ material [32]. The absence of a (200)-magnetic peak discards the noncollinear arrangement of the spins. As predicted by the Yafet-Kittel model, any long-range spin canting (ordering of the transverse component of the magnetic spins) would result in the appearance of the (200)-magnetic Bragg peak [32,34,35]. We do not observe the (200) peak at 21.27° [(400) peak is observed at $2\theta = 43.43°$].

Magnetic moments in different sublattices (M (T_d)—tetrahedral A sites, M (Oct)—octahedral B sites) obtained from refinements are listed in Table I. The resulting magnetic moment per formula unit obtained from NPD refinements is 0.7 (1)μ_B at T = 12 K. However, a discrepancy is observed between the magnetic moments' experimental and theoretical values in the tetrahedral and octahedral sites. Theoretically calculated magnetic moments in different sublattices are M (T_d) $= 0.88 \times 3.87 + 0.12 \times 5.9 = 4.11\mu_B$ and M (Oct) $= 0.87 \times 5.9 + 0.13 \times 3.87) = 5.63\mu_B$, calculated with $M_{Fe}{}^{3+}$ (high spin, $S = 5/2$) $= 5.9\mu_B$ and $M_{Co}{}^{2+}$ ($S = 3/2$) $= 3.87\mu_B$. Reduced magnetic moments could result from local disorder (and/or local canting) of spins. The complex cationic distribution and the existence of nonmagnetic Rh in the structure can originate competing magnetic interactions and can create nonuniform spin canting. A similar reduced magnetic moment due to local spin canting is also observed for the $CoFe_2O_4$ and Ti-doped $CoFe_2O_4$ materials [32,36]. However, a collinear ferrimagnetic long-range magnetic ordering scheme is suggested for both materials.

The temperature variation of the FC and ZFC magnetic susceptibility (χ-T) measured at 0.1 T for $CoFeRhO_4$ is presented in Fig. 5(a). The χ-T shows a sharp upturn at 355 K, highlighting the onset of the ferrimagnetic transition at that temperature. Upon further lowering the temperature, the bifurcation between FC and ZFC susceptibilities (χ_{FC} and χ_{ZFC}) is visible at 220 K. Below 220 K, χ_{FC} shows an increasing trend with decreasing temperature. Several competing magnetic interactions exist in $CoFeRhO_4$. The complex crystal structure (diamond and pyrochlore lattice) and the distribution of mag-

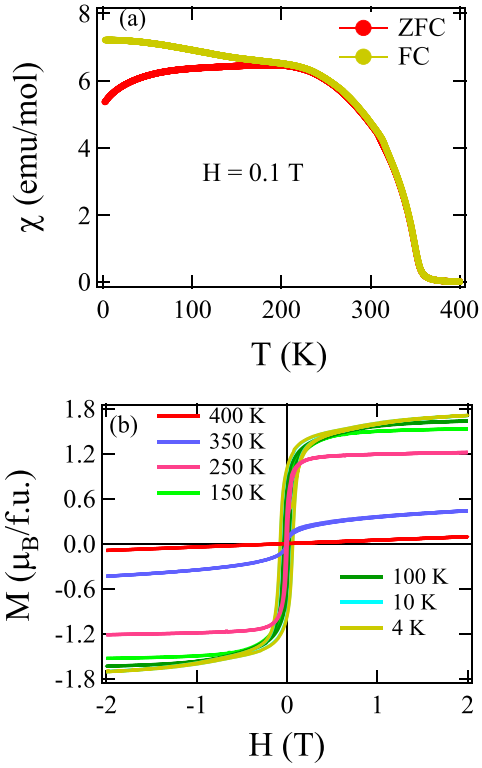

FIG. 5. (a) Temperature-dependent magnetization (M-T) and (b) magnetic-field variation of the magnetization (M-H) for $CoFeRhO_4$. Ferrimagnetic behavior is observed for $CoFeRhO_4$.

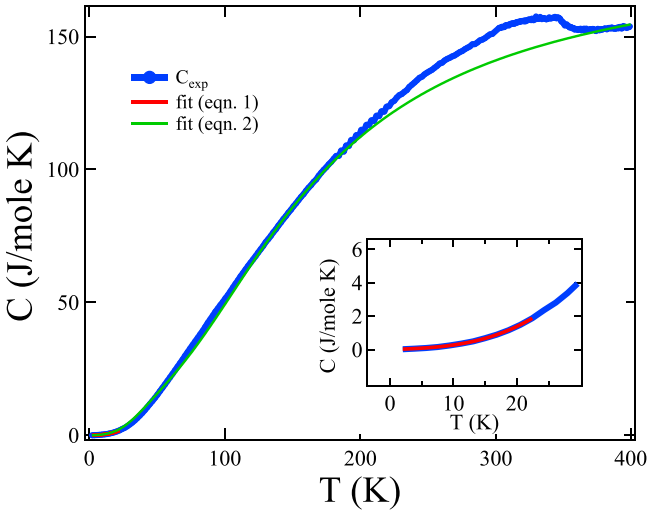

FIG. 6. Temperature variation of the specific heat (C) for $CoFeRhO_4$. An anomaly due to the magnetic ordering is observed at 355 K. The green line highlights the fitted curve using Eq. (2). Low-temperature C is also fitted using Eq. (1) and shown in the inset of the figure.

netic and nonmagnetic cations in two different sublattices can create competing magnetic interactions and frustration. For example, A-site magnetic cations are surrounded by 12 B-site magnetic and nonmagnetic first neighbors, which can be Fe^{3+} or Co^{2+} or Rh^{3+}; any B cation is surrounded by six A- and six B-sited cations. Therefore, the bifurcation and the rise in χ_{FC} at a lower temperature could be due to frustration in the spinel structure. However, the ferrimagnetic transition in $CoFeRhO_4$ is much lower than in $CoFe_2O_4$. In $CoFe_2O_4$, the collinear ferrimagnetic transition is observed at 800 K with a strong intersublattice antiferromagnetic (AFM) superexchange interaction ($J_{AB} = -12.39\ k_B$) [32]. Introducing nonmagnetic Rh into the structure could dilute the magnetic interactions by decreasing the strength of inter- and intrasublattice superexchange interactions and, therefore, can reduce the magnetic ordering temperature. Figure 5(b) shows the magnetization as a function of the magnetic-field (M-H) at various temperatures measured in the ZFC mode. Above the magnetic transition temperature (at 400 K), a linear paramagnetic type M-H behavior is observed. However, at 350 K, the M-H loop illustrates nonlinearity at low magnetic fields, indicating the appearance of the magnetically ordered state. As we further lower the temperature, saturated ferrimagnetic-type M-H loops are observed. The saturation magnetization and coercive field (H_C) enhance with decreasing temperature. The saturation magnetization (M_S) at a temperature of 4 K is $\simeq 1.67\mu_B$/formula unit, surpassing the ordered magnetic moments ($0.7\mu_B$) determined from refinements of NPD (recorded at 12 K). The reduced magnetic moments observed in the NPD refinements could result from local canting of spins [32]. However, applying an external magnetic field aligns a greater number of magnetic spins in the direction of the field, and, therefore, M_S is higher than the ordered magnetic moments.

Figure 6 highlights the temperature variation of total specific heat for $CoFeRhO_4$. Magnetic ordering usually involves an entropy change, resulting in specific-heat anomalies. The C_P vs T plot shows an anomaly at 355 K, indicating a true phase transition. This also confirms the magnetic-ordering temperature for $CoFeRhO_4$. The low-temperature part of the specific heat (2–20 K) can be well represented by Eq. (1),

$$C_P = \gamma T + \beta T^3, \tag{1}$$

where γ = the Sommerfeld coefficient and β = lattice contributions to the specific heat. The obtained $\gamma = 0.015\ \mathrm{J\,mol^{-1}\,K^{-2}}$ and $\beta = 0.000\ 12\ \mathrm{J\,mol^{-1}\,K^{-4}}$. The Debye temperature θ_D is calculated using the expression $\theta_D = (12\pi^4 \mathrm{RN}/5\beta)^{1/3}$ where $R = 8.314\ \mathrm{J\ mol^{-1}\ K^{-1}}$ and $N = 7$, the number of atoms/formula unit. The calculated θ_D gives a value of 327 K. However, the total specific heat at higher temperatures contains both the phonon and the magnetic parts ($C_P = C_{ph} + C_m$). A combined Einstein-Debye model can generally estimate the total phonon contribution in the specific heat. Therefore, to estimate the magnetic contributions (C_m) in the specific heat, we fit the data with the Einstein-Debye model [37],

$$C_{ph} = 9Rx_D^{-3}\int_0^{x_D}\frac{x^4e^x}{(e^x-1)^2}dx + R\sum_{i=1}^{2}a_i\frac{x_{Ei}^2e_{Ei}^x}{\left(e_{Ei}^x-1\right)^2}, \tag{2}$$

where $x_D = \theta_D/T$ and $x_{Ei} = \theta_{Ei}/T$ and, Debye temperature $= \theta_D$ and θ_{Ei} = Einstein temperature. $R = 8.31\ J\ \mathrm{mol^{-1}\ K^{-1}}$), and a_i = degree of freedom for each Einstein mode. The fitted curve is shown in Fig. 6. The best fit is obtained with $\theta_D = 632$, $\theta_{E1} = 177$, and $\theta_{E2} = 740$ K. The θ_D value is obtained from fitting using Eq. (2) is higher than the θ_D calculated using

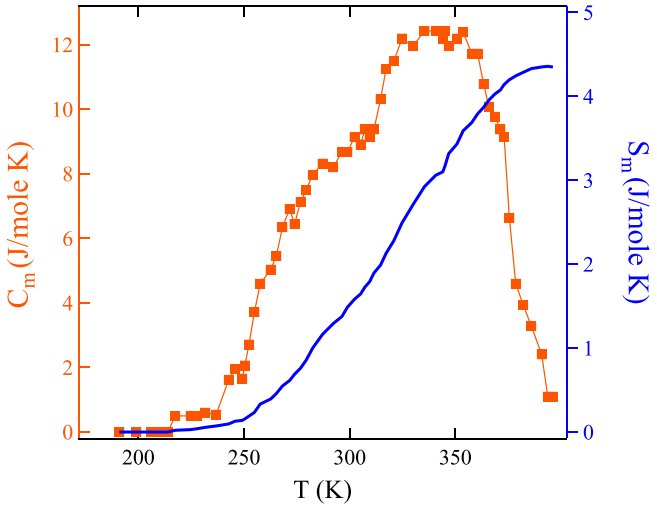

FIG. 7. Temperature variation of the magnetic component of the specific heat (C) (left axis) and calculated magnetic entropy (right axis) for $CoFeRhO_4$.

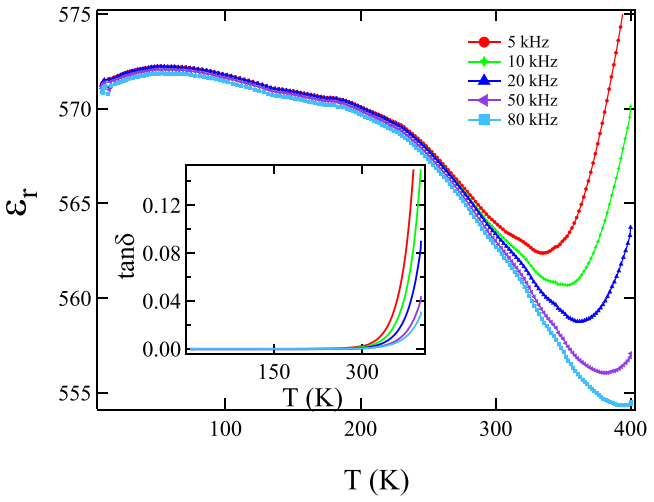

FIG. 8. Temperature variation of the real part of the dielectric constant (ϵ_r) at several fixed frequencies for $CoFeRhO_4$. The inset in the figure shows the dependence of the dielectric loss as a temperature function.

Eq. (1). Then, the contribution related to the magnetic ordering (C_m) in the specific heat is calculated by subtracting C_{ph} from the measured total specific-heat data. Figure 7 highlights the C_m-T plot, showing a sharp maximum at $T = 355$ K. The entropy change due to the magnetic ordering can be calculated by using the following formula:

$$S_m(T) = \int_0^T \frac{C_m(T)}{T} dT. \tag{3}$$

The $S_m(T)$ vs T plot is shown in Fig. 7. Magnetic entropy increases with increasing temperature and shows a saturation value of $\simeq$4.4 J mol^{-1} K^{-1} (above 355 K), and this is less than the theoretically estimated magnetic entropy for $CoFeRhO_4$ [$S_m(T) = R \ln(2S+1) = 26.41$ J mol^{-1} K^{-1}, Co^{2+} adopts the $e_g^4 t_{2g}^3$ electronic configuration with $S = 3/2$, Fe^{3+} adopts the $e_g^2 t_{2g}^3$ electronic configuration with $S = 5/2$). In general, the frustration of the magnetic cations near and above the magnetic transition temperature can reduce the entropy contribution to the magnetic ordering. In $CoFeRhO_4$, geometrical frustration in the structure (diamond and pyrochlore lattices) and the distribution of magnetic and nonmagnetic cations in two different sublattices could cause frustration of magnetic cations. The reduced magnetic moments in the neutron powder diffraction experiments point to spins' local disorder (and/or local canting). Therefore, the reduced entropy related to magnetic ordering can be attributed to the frustration of the magnetic cations [38].

Oxide materials having geometrical frustration and ferrimagnetic transition often result in exciting magnetoelectric/magnetodielectric coupling. Geometric frustration (local spin canting) in a magnetic system is proven to be a key ingredient for magneto(di)electric coupling. For example, the triangular Ising lattice $Ca_3Co_2O_6$ shows magnetodielectric coupling below the ferrimagnetic ordering temperature (24 K) [39]. The Haldane spin-chain system Dy_2BaNiO_5 shows a magneto-(di)electric effect below the long-range ordering temperature (58 K) [40]. In spinels, the magnetodielectric effect is observed from the beginning of the ferrimagnetic ordering in $CoCr_2O_4$ ($T_C = 96$ K) [41,42] and $NiCr_2O_4$ [43]. $MnCr_2O_4$ shows magnetodielectric effect below the ferrimagnetic ordering temperature (43 K) [44]. However, the magneto-(di)electric effect in ferrimagnetic materials near room temperature is rare. The near-room-temperature magnetodielectric effect is essential due to its possible applications in spintronics devices, magnetically accessible ferroelectric random-access memories, and communication technology. Figure 8 shows the temperature variation of the real part of the dielectric constant (ϵ_r) for $CoFeRhO_4$. The dielectric loss ($\tan\delta$) is highlighted in the inset of Fig. 8. The extremely low values of dielectric loss ($\tan\delta$) highlight the insulating behavior of $CoFeRhO_4$. It also excludes the possibility of extrinsic Maxwell-Wagner-like behavior appearing because of the leakage currents. However, the frequency dispersion of ϵ_r and $\tan\delta$ started above 320 K, indicating the growing Maxwell-Wagner-type relaxation or other sources of conductivity around 320 K. However, the dielectric constant is intrinsic below 320 K. In addition to a small hump near the magnetic-ordering temperature (335 K), two anomalies at 220 and 50 K are observed in the ϵ_r-T plots. In particular, the magnetization measurements also show two anomalies at 220 and 50 K.

As observed in our nuclear and magnetic structure refinements, heat capacity, and magnetization studies, $CoFeRhO_4$ hosts an exciting combination of complex crystal structure (diamond and pyrochlore lattice) and competing magnetic interactions. Similar to $CoFe_2O_4$, the reduced magnetic moments observed in the NPD refinements highlight the possibility of local spin canting (noncollinear spins) [32]. The application of the external magnetic field aligns the magnetic spins in the direction of the field, and saturation magnetization is observed >1 T [Fig. 5(b)]. The M-H measurements [Fig. 5(b)] highlight that a magnetic field >1 T is sufficient to align the spins along the field direction by breaking the local canting (noncollinearity). The competing magnetic

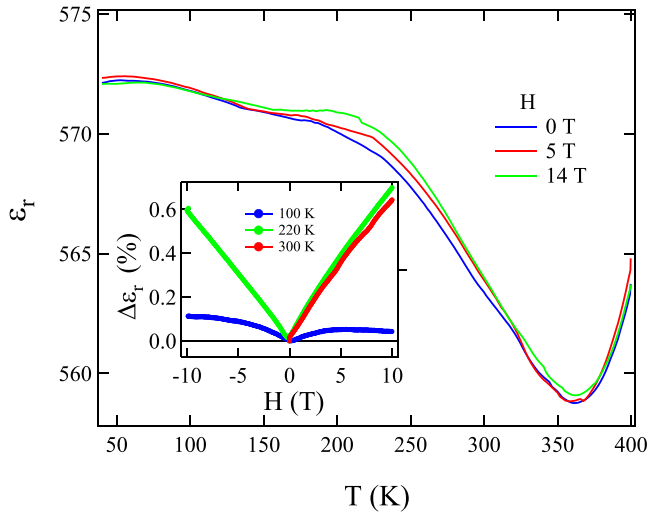

FIG. 9. Temperature-dependent dielectric constant (real part ϵ_r) at different magnetic fields ($H = 0$, 5, and 14 T) for $CoFeRhO_4$. The inset highlights the magnetic-field variation of the dielectric constant $\{\Delta\epsilon_r = [\epsilon_r(H) - \epsilon_r(H = 0)]/\epsilon_r(H = 0)\}$ at different temperatures.

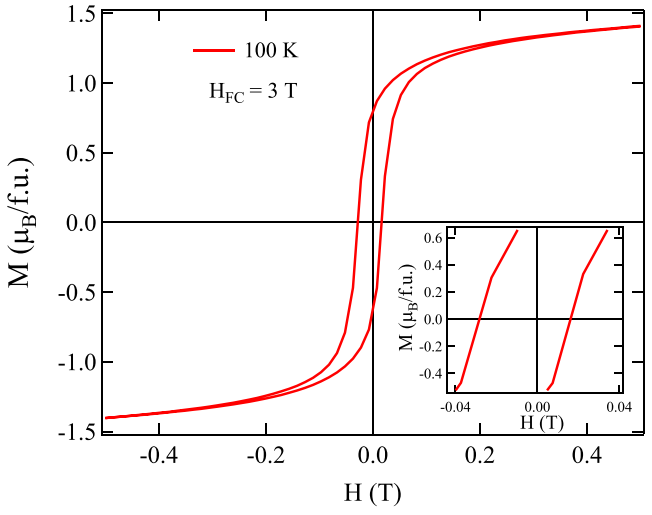

FIG. 10. M-H loop of $CoFeRhO_4$ at 100 K measured in the FC mode ($H_{FC} = 3$ T). The inset highlights the enlarged central part of the FC M-H loop. A shift along the left-field axis is highlighted here.

interactions and the local spin canting can originate magnetic frustration in the structure. Magnetic frustration could be the reason to observe these anomalies below long-range magnetic ordering. To understand the effect of the magnetic field on the dielectric constant, we have performed magnetic-field dependence measurements of the dielectric constant. Figure 9 shows the temperature variation of ϵ_r measured in the presence of different magnetic fields. Interestingly, the dielectric constant increases in the presence of a magnetic field below the magnetic ordering temperature, and a positive magnetodielectrictance effect is observed. The starting of the magneto(di)electric effect below the long-range ferrimagnetic ordering temperature indicates that the observed magneto(di)electric effect is related to the magnetic ordering of $CoFeRhO_4$. The change in the dielectric data with the magnetic field is most pronounced near 220 K. The magnetodielectric constant $[\Delta\epsilon_r = [\epsilon_r(H) - \epsilon_r(H = 0)]/\epsilon_r(H = 0)]$ and its dependence on the magnetic field are shown in the inset of Fig. 9. The maximum value of the magnetodielectric constant is observed near 220 K ($\Delta\epsilon_r = 0.7\%$). In comparison, $CoCr_2O_4$, $NiCr_2O_4$, and $MnCr_2O_4$ show maximum values of the magnetodielectric constant $\simeq 0.02\%$ at 5 K [45]. Cr doping in Mn_2O_3 shows an enhancement in the magnetodielectric effect, however, the maximum value of magnetodielectic constant is $\simeq 0.2\%$ at 5 K [46]. As discussed, the magnetic frustration in the structure (geometric frustration, competing magnetic interactions, and local spin canting) could be the origin of the increase in ϵ_r with the magnetic field at that temperature.

In recent times, complex magnetic materials (for instance, ferrimagnetic systems $Mn_{3-x}Pt_xGa$ [47], $Ba_2Fe_{1.12}Os_{0.88}O_6$ [48], and $SrFe_{0.15}Co_{0.85}O_{2.62}$) [49], in particular, those having a magnetic transition temperature near room temperature, have attracted significant interest in exploring the EB. The EB effect shifts the isothermal magnetization loop, becoming asymmetric and shifting along the field axis. This effect has important technological applications, such as in the development of magnetic sensors, magnetic recording read heads [50], random access memories [51], and other spintronic devices [52,53]. Figure 10 highlights the magnetic-field dependence of magnetization at 100 K, measured in FC mode (cooling field $H_{FC} = 3$ T). It shows a clear shift towards the left field (negative magnetic field). The EB field (H_{EB}) can be calculated from the shift of the hysteresis loop using the following equation:

$$H_{EB} = -(H_{C(L)} + H_{C(R)})/2, \tag{4}$$

($H_{C(L)}$ and $H_{C(R)}$ are the intercepts with the positive (right) and negative (left) field axis. The calculated exchange bias field $H_{EB} = 65$ Oe at 100 K. The exchange bias field is almost constant with varying cooling fields (H_{FC}, ranging from 1 to 7 T). To investigate the temperature evolution of the exchange bias effect and to explore whether the exchange bias property in $CoFeRhO_4$ is correlated with magnetic ordering, we have measured the temperature variation of the EB field. The material was cooled to the measuring temperatures in a magnetic field of 3 T. Then, the M-H loops were measured between ± 0.5 T. Figure 11 highlights the temperature evolution of the EB field for $CoFeRhO_4$. Interestingly, the EB effect emerges just below the long-range ferrimagnetic ordering (350 K); however, with decreasing temperature, H_{EB} shows almost constant behavior down to 10 K. In ferrimagnetic systems, the presence of uncompensated magnetic moments in a compensated AFM host is proven to be very effective in designing the exchange bias effect (for instance, $Mn_{3-x}Pt_xGa$ [47], $Ba_2Fe_{1.12}Os_{0.88}O_6$) [48]. In this spinel structure, there is an uncompensated magnetic moment due to the distribution of two different magnetic cations (Co^{2+} and Fe^{3+}) in two different sublattices. In $CoFeRhO_4$, as observed from the neutron diffraction refinements (Table I), below the magnetic-ordering temperature, the magnetic moment of the B sublattice [M (Oct)] dominates over the M (T_d). Under FC conditions, the magnetic field orients the net magnetic

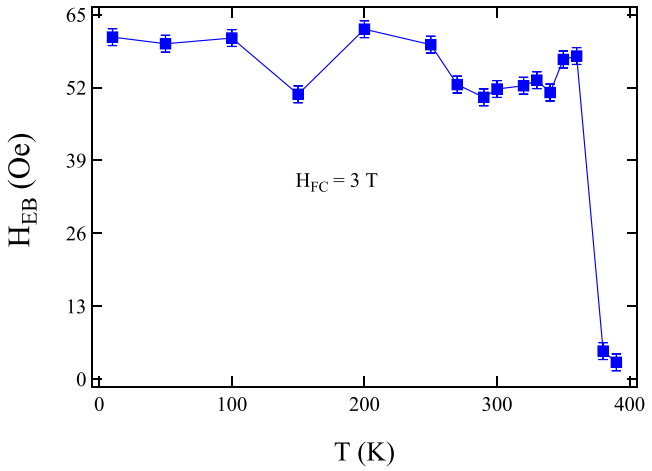

FIG. 11. Temperature variation of the exchange bias field (H_{EB}) for $CoFeRhO_4$. The exchange bias effect started to appear below the long-range ferrimagnetic ordering (350 K).

moment of the sublattices along the field direction. Now, as we gradually reverse the direction of the magnetic field, the magnetic moments of the B sublattice [M (Oct)] do not easily reverse its direction as they are antiferromagnetically coupled with the A-sublattice [M (T_d)] This pining effect of irreversible uncompensated spins (octahedral B sublattice) develops unidirectional anisotropy, and, therefore, exchange bias is observed in $CoFeRhO_4$.

IV. CONCLUSION

To summarize, we synthesized and examined the detailed structural, magnetic, thermal (specific-heat), magnetodielectric, and magnetic exchange bias properties of $CoFeRhO_4$, a mixed $3d$-$4d$ spinel oxide. We used various diffraction techniques, such as RT-XRD, NPD, RT-electron diffraction, and STEM, to explore the material's structural details. The material crystallizes in a cubic structure with a space group of $Fd\bar{3}m$. Our measurements show a long-range ferrimagnetic ordering with an onset at 355 K, which is explained by a collinear ferrimagnetic ordering model with $k = [0, 0, \text{and } 0]$. However, we observe reduced magnetic moments in the refinement, possibly due to the spins, local disorder, local canting, or frustration. Magnetic frustration can also reduce magnetic entropy as reflected in the specific-heat measurement. The magnetic entropy increases with temperature and reaches a saturation value of 4.4 J $mol^{-1} K^{-1}$ (above 355 K) but is less than the theoretically estimated value. Furthermore, our dielectric and FC magnetization measurements show the appearance of two technologically significant phenomena near room temperature: the magnetodielectric effect and the exchange bias effect. These effects appear below the magnetic ordering temperature (355 K) and can originate from magnetic frustration, collinear ferrimagnetic ordering, and uncompensated magnetic moments. The uncompensated magnetic moments create unidirectional anisotropy, resulting in an exchange bias effect. Importantly, the presence of room-temperature ferrimagnetism, EB, and the magneto(di)electric effect demonstrates the potential of $CoFeRhO_4$ in the development of materials for sensors or spintronics applications operating at room temperature.

ACKNOWLEDGMENTS

R.P.S. acknowledges the Science and Engineering Research Board (SERB), Government of India, for the CRG/2019/001028 Core Research Grant. S.M. acknowledges the SERB, Government of India, for the SRG/2021/001993 Start-up Research Grant.

[1] V. W. J. Verhoeven, F. M. Mulder, and I. M. De Schepper, Physica B **276-278**, 950 (2000).
[2] V. Kocsis, S. Bordács, D. Varjas, K. Penc, A. Abouelsayed, C. A. Kuntscher, K. Ohgushi, Y. Tokura, and I. Kézsmárki, Phys. Rev. B **87**, 064416 (2013).
[3] V. Fritsch, J. Hemberger, N. Buttgen, E.-W. Scheidt, H.-A. Krug von Nidda, A. Loidl, and V. Tsurkan, Phys. Rev. Lett. **92**, 116401 (2004).
[4] R. Fichtl, V. Tsurkan, P. Lunkenheimer, J. Hemberger, V. Fritsch, H.-A. Krug von Nidda, E.-W. Scheidt, and A. Loidl, Phys. Rev. Lett. **94**, 027601 (2005).
[5] D. Santos-Carballal, A. Roldan, R. Grau-Crespo, and N. H. de Leeuw, Phys. Rev. B **91**, 195106 (2015).
[6] U. Lüders, A. Barthelemy, M. Bibes, K. Bouzehouane, S. Fusil, E. Jacquet, J.-P. Contour, J.-F. Bobo, J. Fontcuberta, and A. Fert, Adv. Mater. **18**, 1733 (2006).
[7] Q. Zhang, W. Tian, R. Nepal, A. Huq, S. Nagler, J. F. Ditusa, and R. Jin, Chem. Mater. **35**, 2330 (2023).
[8] Z. Chi, F.-G. Tarntair, M. Fregnaux, W.-Y. Wu, C. Sartel, I. Madaci, P. Chapon, V. Sallet, Y. Dumont, A. Perez-Tomas, R. H. Horng, and E. Chikoidze, Mater. Today Phys. **20**, 100466 (2021).
[9] D. Gao, Q. Kuang, F. Gao, H. Xin, S. Yun, and Y. Wang, Mater. Today Phys. **27**, 100765 (2022).
[10] J. Li, J. Li, D. Chu, H. Dong, D. R. Baker, and R. Jiang, J. Am. Chem. Soc. **142**, 50 (2020).
[11] R. Eppstein and M. Caspary Toroker, ACS Mater. Au **2**, 269 (2022).
[12] Ö. N. Avcı, L. Sementa, and A. Fortunelli, ACS Catal. **12**, 9058 (2022).
[13] G. Liang, E. Olsson, J. Zou, Z. Wu, J. Li, C.-Z. Lu, A. M. D'Angelo, B. Johannessen, L. Thomsen, B. Cowie, V. K. Peterson, Q. Cai, W. K. Pang, and Z. Guo, Angew. Chem. Int. Ed. **61**, e202201969 (2022).
[14] W. Xiang, N. Yang, X. Li, J. Linnemann, U. Hagemann, O. Ruediger, M. Heidelmann, T. Falk, M. Aramini, S. DeBeer, M. Muhler, K. Tschulik, and T. Li, Nat. Commun. **13**, 179 (2022).
[15] M. L. Neel, Ann. Phys. (Paris) **12**, 137 (1948).
[16] D. Das and S. Ghosh, J. Phys. D: Appl. Phys. **48**, 425001 (2015).

[17] S.-H. Lee, C. Broholm, T. H. Kim, W. Ratcliff II, and S.-W. Cheong, Phys. Rev. Lett. **84**, 3718 (2000).
[18] J.-H. Chung, M. Matsuda, S.-H. Lee, K. Kakurai, H. Ueda, T. J. Sato, H. Takagi, K.-P. Hong, and S. Park, Phys. Rev. Lett. **95**, 247204 (2005).
[19] Y. Yamasaki, S. Miyasaka, Y. Kaneko, J.-P. He, T. Arima, and Y. Tokura, Phys. Rev. Lett. **96**, 207204 (2006).
[20] See Supplemental Material at https://link.aps.org/supplemental/10.1103/PhysRevMaterials.7.084408 for that includes information on the Rietveld refinement of XRD, neutron diffraction (ND) at 100 K, and nuclear structure analysis of ND at 250 K.
[21] L. Ge, J. Flynn, J. A. M. Paddison, M. B. Stone, S. Calder, M. A. Subramanian, A. P. Ramirez, and M. Mourigal, Phys. Rev. B **96**, 064413 (2017).
[22] J. R. Chamorro, L. Ge, J. Flynn, M. A. Subramanian, M. Mourigal, and T. M. McQueen, Phys. Rev. Mater. **2**, 034404 (2018).
[23] S. Das, D. Nafday, T. Saha-Dasgupta, and A. Paramekanti, Phys. Rev. B **100**, 140408 (2019).
[24] H. Cho, R. Nirmala, J. Jeong, P. J. Baker, H. Takeda, N. Mera, S. J. Blundell, M. Takigawa, D. T. Adroja, and J.-G. Park, Phys. Rev. B **102**, 014439 (2020).
[25] M. S. Akbar, M. A. Rafiq, A. Javed, M. N. Rasul, M. A. Khan, and A. Hussain, J. Magn. Magn. Mater. **572**, 170604 (2023)
[26] D. Bergman, J. Alicea, E. Gull, S. Trebst, and L. Balents, Nat. Phys. **3**, 487 (2007).
[27] B. Zager, J. R. Chamorro, L. Ge, F. Bahrami, V. Bisogni, J. Pelliciari, J. Li, G. Fabbris, T. M. McQueen, M. Mourigal, and K. W. Plumb, Phys. Rev. B **106**, 045134 (2022).
[28] F. L. Buessen, M. Hering, J. Reuther, and S. Trebst, Phys. Rev. Lett. **120**, 057201 (2018).
[29] M. K. Wallace, Jun Li, P. G. Labarre, S. Svadlenak, D. Haskel, J. Kim, G. E. Sterbinsky, F. Rodolakis, H. Park, A. P. Ramirez, and M. A. Subramanian, Phys. Rev. Mater. **5**, 094410 (2021).
[30] G. Chen, Phys. Rev. B **96**, 020412 (2017).
[31] A. V. Zakrzewski, S. Gangopadhyay, G. J. MacDougall, A. A. Aczel, S. Calder, and T. J. Williams, Phys. Rev. B **97**, 214411 (2018).
[32] J. Teillet, F. Bouree, and R. Krishnan, J. Magn. Magn. Mater. **123**, 93 (1993).
[33] J. W. Kim, D. H. An, S. K. Chang, H. L. Ju, K. S. Baek, H. N. Oak, and H. S. Lee, J. Phys. Chem. Solids **63**, 241 (2002).
[34] H. Parmar, P. Acharya, R. V. Upadhyay, and V. Siruguri, and S. RayaprolSolid State Commun. **153**, 60 (2013).
[35] N. S. S. Murthy, M. G. Natera, S. L. Youssef, and R. J. Begum, Phys. Rev. **181**, 969 (1969).
[36] J. L. Dormann, M. E. Harfaoui, M. Nogues, and J. Jove, J. Phys. C: Solid State Phys. **20**, L161 (1987).
[37] Y. Ikedo, J. Sugiyama, H. Nozaki, H. Itahara, J. H. Brewer, E. J. Ansaldo, G. D. Morris, D. Andreica, and A. Amato, Phys. Rev. B **75**, 054424 (2007).
[38] R. P. Singh and C. V. Tomy, Phys. Rev. B **78**, 024432 (2008).
[39] T. Basu, K. K. Iyer, P. L. Paulose, and E. V. Sampathkumaran, J. Alloys Compd. **675**, 364 (2016).
[40] K. Singh, T. Basu, S. Chowki, N. Mahapotra, K. K. Iyer, P. L. Paulose, and E. V. Sampathkumaran, Phys. Rev. B **88**, 094438 (2013).
[41] S. Yang, H. X. Bao, D. Z. Xue, C. Zhou, J. H. Gao, Y. Wang, J. Q. Wang, X. P. Song, Z. B. Sun, and X. B. Ren, J. Phys. D: Appl. Phys. **45**, 265001 (2012).
[42] A. Sethi, T. Byrum, R. D. McAuliffe, S. L. Gleason, J. E. Slimak, D. P. Shoemaker, and S. L. Cooper, Phys. Rev. B **95**, 174413 (2017).
[43] C. M. Zhu, G. B. Yu, L. G. Wang, M. W. Yao, F. C. Liu, and W. J. Kong, J. Magn. Magn. Mater. **506**, 166803 (2020).
[44] N. Mufti, G. R. Blake, and T. T. M. Palstra, J. Magn. Magn. Mater. **321**, 1767 (2009).
[45] N. Mufti, A. A. Nugroho, G. R. Blake, and T. T. M. Palstra, J. Phys.: Condens. Matter **22**, 075902 (2010).
[46] M. Chandra, S. Yadav, R. Rawat, and K. Singh, J. Phys.: Condens. Matter **32**, 295703 (2020).
[47] A. K. Nayak, M. Nicklas, S. Chadov, P. Khuntia, C. Shekhar, A. Kalache, M. Baenitz, Y. Skourski, V. K. Guduru, A. Puri, U. Zeitler, J. M. D. Coey, and C. Felser, Nature Mater. **14**, 679 (2015).
[48] H. L. Feng, P. Adler, M. Reehuis, W. Schnelle, P. Pattison, A. Hoser, C. Felser, and M. Jansen, Chem. Mater. **29**, 886 (2017).
[49] P. Mohanty, S. Marik, D. Singh, and R. P. Singh, Appl. Phys. Lett. **111**, 022402 (2017).
[50] W. H. Meiklejohn and C. P. Bean, Phys. Rev. **102**, 1413 (1956).
[51] R. E. Ching Tsang, R. E. Fontana, T. Lin, D. Heim, V. S. Speriosu, B. A. Gurney, and M. L. Williams, IEEE Trans. Magn. **30**, 3801 (1994).
[52] I. L. Prejbeanu, M. Kerekes, R. C. Sousa, H. Sibuet, O. Redon, B. Dieny, and J. P. Nozi‘eres, J. Phys.: Condens. Matter **19**, 165218 (2007).
[53] Y. T. Chen, S. U. Jen, Y. D. Yao, J. M. Wu, J. H. Liao, and T. B. Wu, J. Alloys Compd. **448**, 59 (2008).